COMMUNICATIONS PHYSICS

ARTICLE

https://doi.org/10.1038/s42005-020-0372-9 OPEN

$SrNbO_3$ as a transparent conductor in the visible and ultraviolet spectra

Yoonsang Park[1], Joseph Roth[1], Daichi Oka[2], Yasushi Hirose[3], Tetsuya Hasegawa[3], Arpita Paul[4], Alexej Pogrebnyakov[1], Venkatraman Gopalan[1,5], Turan Birol[4] & Roman Engel-Herbert[1,5,6]✉

Few materials have been identified as high-performance transparent conductors in the visible regime (400–700 nm). Even fewer conductors are known to be transparent in ultraviolet (UV) spectrum, especially at wavelengths below 320 nm. Doped wide-bandgap semiconductors employed currently as UV transparent conductors have insufficient electrical conductivities, posing a significant challenge for achieving low resistance electrodes. Here, we propose $SrNbO_3$ as an alternative transparent conductor material with excellent performance not only in the visible, but also in the UV spectrum. The high transparency to UV light originates from energetic isolation of the conduction band, which shifts the absorption edge into the UV regime. The standard figure of merit measured for $SrNbO_3$ in the UV spectral range of 260–320 nm is on par with indium tin oxide in the visible, making $SrNbO_3$ an ideal electrode material in high-performance UV light emitting diodes relevant in sanitation application, food packaging, UV photochemotherapy, and biomolecule sensing.

[1] Department of Materials Science and Engineering, The Pennsylvania State University, University Park, PA 16802, USA. [2] Department of Chemistry, Graduate School of Science, Tohoku University, Sendai 980-8578, Japan. [3] Department of Chemistry, School of Science, The University of Tokyo, 7-3-1 HongoBunkyoTokyo 113-0033, Japan. [4] Department of Chemical Engineering and Materials Science, University of Minnesota, Minneapolis, MN 55455, USA. [5] Department of Physics, The Pennsylvania State University, University Park, PA 16802, USA. [6] Department of Chemistry, The Pennsylvania State University, University Park, PA 16802, USA. ✉email: rue2@psu.edu

The demand for high performance transparent conductor materials has significantly increased because the unique combination of electrical and optical properties—allowing light to effectively cross the path of electric conduction—is needed for top electrodes used in light emitting diodes (LEDs), photovoltaic cells and optical detectors. Up until now, the focus has been on high optical transparency in the visible spectrum while maintaining a high electrical conductivity. Many applications require shorter wavelength light, such as solar blind detection in the range of 240–280 nm[1], ultraviolet (UV) curing (260–320 nm)[2], biomolecule sensing (250–400 nm)[3], UV germicidal irradiation in the upper UV range (260–280 nm)[4], UV lithography (248 nm)[5], UV phototherapy (ultraviolet B (UVB), 280–315 nm)[6], photochemotherapy (ultraviolet A (UVA), 315–400 nm)[7], and light sources for plant growth stimulating the secondary metabolism by exposure to radiation in UVB[8]. This wide application space has driven research in the area of UV LEDs as environmentally benign alternative over conventional UV light sources, such as low-pressure mercury lamps, offering higher efficiency, longer lifetime, and fast switching[9,10].

In contrast to the high external quantum efficiencies (EQEs) of 45–96% achieved for LEDs emitting in the visible (400–700 nm) and UVA spectrum[11–15], LEDs emitting deeper in the UV have significantly lower EQEs of only around 1%[16–19], attributed to poor hole injection[20], and high defect densities of the wide band gap semiconductor in the active region[21]. Another roadblock towards a higher EQE is the lack of a transparent electrode material with high electrical conductivity and high optical transparency in the deeper UV range that has similar performance to transparent conductors in the visible[22]. Indium–tin oxide (ITO), which is the most widely used transparent electrode, has a strong absorption edge near 360 nm rendering it unsuitable as a UV transparent electrode[23,24]. Currently proposed visible transparent conductors, such as oxide-metal-oxide heterostructures, e.g. ITO/Cu/ITO or indium zinc oxide (IZO)/Ag/IZO[25,26], transparent conducting oxide (TCOs), such as Zn–In–Sn–O multicomponent oxides and indium-free Al and Ga-doped ZnO films[27,28], and ultrathin metallic films, such as Ag, Ni and Cr[29–31], lack high transmittance in the deep UV region. Considerable efforts have been undertaken to synthesize deep UV transparent conductor thin films by utilizing ultrawide bandgap semiconductors, such as β-Ga_2O_3[32,33] and $ZnGa_2O_4$[34,35]. Although these materials possess high transmittance in the UV range due to their large band gaps of about 4.5[36] and 5.0 eV[37], respectively, their electrical conductivities are orders of magnitude lower than degenerately doped ITO. Given the lack of high performance UV transparent conductors, recent improvements of UV LEDs have been achieved utilizing costly flip-chip designs[38], in which a metal reflector enhances the light extraction by guiding the emission towards transparent sapphire substrate, resulting in increased EQEs typically ranging between 3% and 10%[39–41], and up to 20% EQE at a wavelength of 275 nm[42]. Ultimately, alternative materials options for UV transparent electrodes are needed to enhance EQEs of UV LEDs[43,44].

We propose the correlated metal $SrNbO_3$ as an alternative UV transparent conductor that shows excellent performance in both the visible and the UV regime from 260 to 320 nm. The design rule of this UV transparent conductor is based on taking advantage of the energetically isolated conduction band originating from the Nb 4*d* orbitals, and a sizeable electron correlation present in $SrNbO_3$, as first proposed by Zhang et al for the vanadates in the visible spectrum[45]. In correlated metals, many-body effects arising from strong electron-electron interactions affect transport properties and optical response of the carriers and are quantified by the renormalization constant Z_k. If the electron interaction strength is negligible ($Z_k = 1$), itinerant carriers respond like a free electron gas; if $Z_k = 0$ as a consequence of a strong electron interaction, all free carriers are localized at lattice sites (Mott insulator); and if the renormalization constant is between these limiting cases ($0 < Z_k < 1$) electrons maintain their itinerant character but their dynamic properties, such as the carrier effective mass m^*, have to be renormalized[46]. For correlated metals the effective mass $m^* = m_b^*/Z_k$ is increased relative to the band effective mass m_b^* by the inverse of the renormalization constant. As a consequence, the reduced plasma frequency $\omega_p = \left(e/\sqrt{\varepsilon_0\varepsilon_r}\right) \cdot \sqrt{Z_k \cdot n/m_b^*}$ is shifted towards the IR despite a metal-like carrier concentration n, with ε_0 and ε_r the vacuum and relative permittivity, and e the elemental charge. Although the increase in effective mass somewhat reduces the electrical conductivity $\sigma = en\mu = e^2\tau\left(n/m^*\right)$, with carrier mobility μ and electron scattering time τ, typical electrical conductivities[45,47] of correlated metals were found to be about one order of magnitude higher than that of ITO and more than three orders of magnitude higher than those of doped β-Ga_2O_3[33,48] and $ZnGa_2O_4$[34,35].

While correlated oxides with perovskite structure, like $SrVO_3$, were experimentally verified as an excellent alternative to conventional transparent conductors, the absorption edge was located at about 2.9 eV (427 nm), causing a sizeable loss in the average optical transparency in the visible range. The large absorption was identified to originate from an interband transition from oxygen 2*p* bands forming the valence band to the unoccupied states of the conduction band derived from the t_{2g} orbitals of the transition metal element vanadium. This interband absorption edge could be potentially shifted to higher energy if the electronegativity difference (Δχ) between the transition metal cation and oxygen anion would be larger. Choosing a less electronegative transition metal with larger Δχ to oxygen and similar electronic configuration would increase the energy difference between O 2*p* and transition metal t_{2g} bands, causing the absorption edge to occur at higher photon energies. Replacing the vanadium cation (V^{4+}) by the isoelectronic niobium (Nb^{4+}) with a smaller electronegativity of niobium (1.690 for Nb^{4+} compared to 1.795 for V^{4+})[49], Δχ becomes larger by ~6% and the transparent window can potentially be widened by pushing the absorption edge beyond the visible and into the UV regime. Upon substituting vanadium by niobium not only a blue-shift of the absorption edge, but also a reduction of the electron correlation strength is expected. The size of *d*-orbitals is larger for Nb^{4+} compared to V^{4+}, so that the orbital overlap and thus the bandwidth W of the conduction band is larger for $SrNbO_3$ despite its larger lattice parameter of a = 4.02 Å, compared to $SrVO_3$ with $a = 3.84$ Å. The consequence of a smaller electron correlation strength is a renormalization constant closer to unity, and thus a smaller m*. This in turn decreases the correlation induced red-shift of the reduced plasma frequency and might reduce optical transparency of $SrNbO_3$ at long wavelengths of the visible spectrum.

Here we present a combined first principles calculation and experimental study to demonstrate the potential of $SrNbO_3$ as UV transparent conductor material. A thickness series of $SrNbO_3$ films was grown and electrical properties were determined from Hall effect and conductivity measurements. The dielectric function of $SrNbO_3$ was measured using spectroscopic ellipsometry and electron correlation strength was extracted applying the extended Drude model. Good agreement between experiment and theoretical prediction was obtained. The figure of merit for transparent conductors was determined for $SrNbO_3$ in the visible and UV spectral range from 260 to 320 nm to be in the range of mid and low $10^{-3}\,\Omega^{-1}$, respectively. These values are comparable with indium–tin oxide in the visible, but one order of magnitude higher in the UV, rendering $SrNbO_3$ as superior transparent conductor in this spectral range.

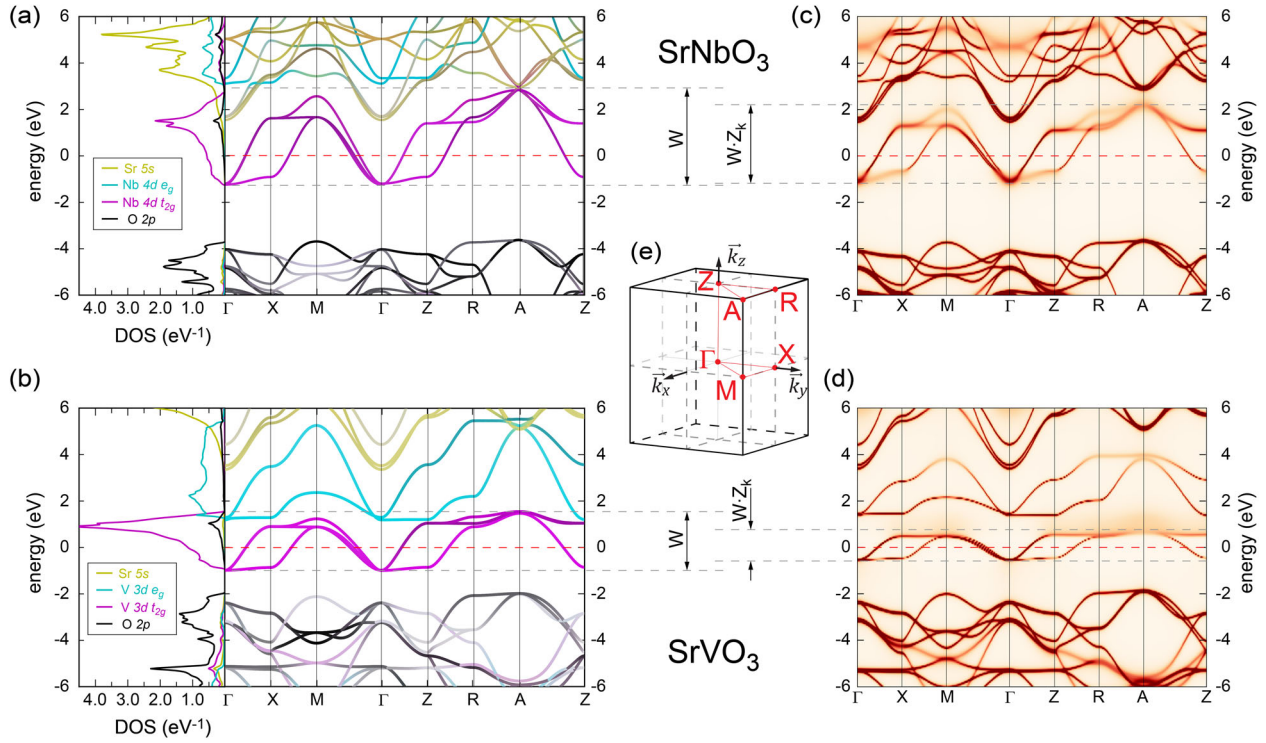

Fig. 1 Electronic properties of correlated metals $SrNbO_3$ and $SrVO_3$. **a** Density of states (DOS) and band structure of $SrNbO_3$ calculated by density functional theory (DFT) under compressive strain ($a = 3.98$ Å). The colors correspond to the orbital character of the bands. **b** DOS and band structure of $SrVO_3$ calculated by DFT under tensile strain ($a = 3.88$ Å). The colors correspond to the orbital character of the bands. **c** Spectral function of $SrNbO_3$ calculated by DFT and dynamical mean field theory (DMFT). The conduction band width W is reduced by the renormalization constant Z_k compared to the DFT results in **a**. **d** Spectral function of $SrVO_3$ calculated by DFT and DMFT. The conduction band width W is reduced by the renormalization constant Z_k compared to the DFT results in **b**. **e** Schematic of the 1st Brillouin zone for tetragonally distorted $SrNbO_3$ and $SrVO_3$.

Results

Density functional theory and dynamical mean field theory. Motivated by these trends we performed density functional theory (DFT) and dynamical mean-field theory (DMFT) calculations to quantify the potential of $SrNbO_3$ as a visible and UV transparent conductor[50,51], Fig. 1a shows the calculated band structure of $SrNbO_3$, which is found to be qualitatively similar to isoelectronic $SrVO_3$ seen in Fig. 1b. Three bands originated from the t_{2g} manifold of the Nb 4*d* orbital were intersected by the Fermi level, giving rise to metallic conduction. The valence bands derived from the O *2p* orbitals were well below the Nb 4*d* bands. An energy gap between the valence band maximum and the conduction band minimum of about 2.3 eV was obtained, considerably larger than the energy gap calculated for $SrVO_3$ of about 1 eV. The interband absorption edge originated from a strong interband transition, either from occupied states of the O 2*p* bands to unoccupied states of Nb 4*d* t_{2g} bands or from occupied states of Nb 4*d* t_{2g} bands below the Fermi level to higher lying unoccupied bands derived from the Nb 4*d* e_g and Sr 5*s* orbitals. For electrons to transition between occupied O 2*p* and unoccupied Nb 4*d* t_{2g} states photon energies larger than 4 eV were needed, while interband transition energies from occupied Nb 4*d* t_{2g} to unoccupied Nb 4*d* e_g and Sr 5*s* states were ~2.5–3 eV. The energy separation between the individual bands was considerably larger compared to $SrVO_3$, where transitions from occupied O *2p* to unoccupied V *3d* t_{2g} states already occurred at about 2.7 eV, while interband transition energies from occupied V *3d* t_{2g} to unoccupied V 3*d* e_g already occurred at about 2.2 eV, albeit with a small dipole matrix element[45]. The direct comparison of DFT results with DMFT calculations for $SrNbO_3$ (Fig. 1a, c) and $SrVO_3$ (Fig. 1b, d) also confirmed the reduced correlation strength of $SrNbO_3$, resulting in a larger renormalization constant ($Z_k \sim 0.72$) and thus a smaller overall reduction of the conduction band width *W* compared to $SrVO_3$ ($Z_k \sim 0.55$)[52]. This is seen by comparing the conduction band widths obtained from DFT and DMFT for both materials shown in Fig. 1. For clarity the 1st Brillouin zone of tetragonally distorted perovskite crystals is shown in Fig. 1e. The reduced correlation strength in $SrNbO_3$ was attributed to the increased size of the 4*d* orbitals compared to 3*d* orbitals in $SrVO_3$, giving rise to a larger orbital overlap despite a larger lattice parameter. The correlation induced red-shift of the reduced plasma frequency marking the reflection edge of carriers is therefore somewhat smaller for $SrNbO_3$.

Electrical Characterization of $SrNbO_3$ Thin Films. After confirming the potential of $SrNbO_3$ as a transparent conductor using first principle calculations, we experimentally investigated the electrical and optical properties of $SrNbO_3$ by growing a series of films with varying thickness on $KTaO_3$ substrates. The sheet resistance (R_s) as a function of thickness is shown in Fig. 2a. The line fitted through the data takes into account the Fuchs-Sondheimer effect[53,54] for electron surface scattering (see Supplementary Note 1). The $SrNbO_3$ films with thicknesses in the range of 10–60 nm had sheet resistance values between 67.5 Ω/sq and 7.3 Ω/sq and the films' electrical resistivities varied between 6.9×10^{-5} Ω cm and 3.8×10^{-5} Ω cm. The variation was attributed to a larger surface scattering contribution for thinner films. Note that the residual resistivity ratios (RRR) were relatively small, as can be seen from the temperature dependent resistivity curves for $SrNbO_3$ films with 23 nm and 37 nm thickness, shown in the inset of Fig. 2a. The RRR values were 1.6 and 3.2,

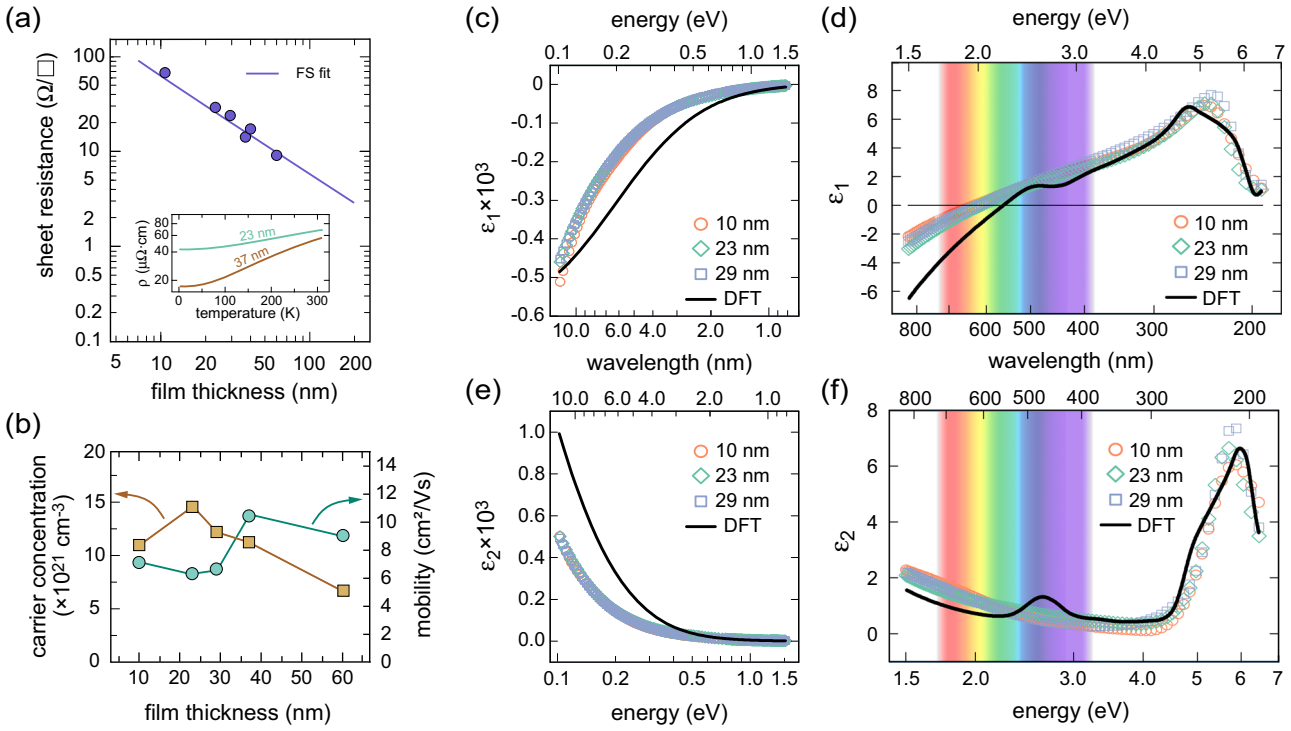

Fig. 2 Electrical and optical properties of $SrNbO_3$ films. a Room temperature sheet resistance of $SrNbO_3$. The line represent a fit for all films taking into account electron surface scattering using the Fuchs-Sondheimer[53, 54] model. Inset shows temperature dependent resistivity for $SrNbO_3$ films with 23 and 37 nm thickness. **b** Carrier concentration (left axis) and carrier mobility (right axis) of $SrNbO_3$ films at room temperature. **c**, **d** Real (ε_1) and **e**, **f** complex (ε_2) part of the dielectric function measured for $SrNbO_3$ films in the infrared range, **c**, **e** and the visible and ultraviolet range, **d**, **f** and calculated by density functional theory (DFT). Rainbow color in the background highlight the visible range. Note different scale between the infrared in **c**, **e**, and the visible to ultraviolet range **d**, **f**. Errors determined from the fit of the optical model are shown in Supplementary Table 1.

respectively, indicating that temperature independent scattering from defects significantly affected the electric conductivity. Nevertheless the sheet resistance values measured for $SrNbO_3$ thin films are comparable to sheet resistance values of other high-performance transparent conductors in the visible spectrum[28,29,45,55,56] and were about three orders of magnitude lower compared to current UV transparent conductor materials[32,35]. Figure 2b show thickness dependence of carrier mobility μ and carrier concentration n for the $SrNbO_3$ thin films. An average mobility value of ~8 $cm^2\,V^{-1}\,s^{-1}$ was determined at room temperature, comparable to values of other correlated metals, such as $SrVO_3$ and $CaVO_3$[45], and about an order of magnitude lower than those of ITO and conventional TCOs[28]. Typical carrier concentrations were around 1×10^{22} cm^{-3}, about a factor of two smaller than carrier concentration measured for $SrVO_3$, but over one order of magnitude higher than conventional TCOs, and UV transparent conductor in particular. While the highest carrier concentration reported for Ga_2O_3 was on the order of low 10^{20} cm^{-3} with a carrier mobility of 50 $cm^2\,V^{-1}\,s^{-1}$ [57,58], typical values for $ZnGa_2O_4$ were similar with carrier concentrations not higher than 10^{20} cm^{-3} and carrier mobilities of ~80 cm2 $V^{-1}\,s^{-1}$ [59]. The much lower carrier mobility of $SrNbO_3$ was overcompensated by the high carrier concentration present, giving rise to superior electrical properties compared to conventional UV transparent conductors. The relatively small effect of resistivity increase arising from surface scattering in $SrNbO_3$ is attributed to the short electron mean-free path (EMFP) Λ, which was estimated using the Sommerfeld model and experimental values for carrier mobility and carrier concentration: $\Lambda = \frac{\hbar \cdot \mu}{e}(3\pi^2 n)^{1/3}$ (see Supplementary Note 1)[60]. For the films investigated an average EMFP of (3.5 ± 0.7) nm was found, which was comparable to those of transparent correlated metals $SrVO_3$ (Λ = 5.6 nm) and $CaVO_3$ (Λ = 3.9 nm)[45], but much lower than those of conventional metals, such as silver (Λ = 52 nm)[61]. This small EMFP allows for more aggressive thickness scaling.

Optical characterization of $SrNbO_3$ thin films. Optical properties of $SrNbO_3$ films were characterized by spectroscopic ellipsometry at room temperature. Figure 2c–f show the complex dielectric function ($\varepsilon = \varepsilon_1 + i\varepsilon_2$) measured for three $SrNbO_3$ films with thicknesses of 10, 23 and 29 nm. In addition, the dielectric function calculated from DFT is shown for comparison as well. Fig. 2c, e show the real and imaginary part of the dielectric function in the infrared (IR) range from 20 μm down to 800 nm, Fig. 2d and f show ε_1 and ε_2 from 800 nm down to 200 nm across the entire visible range all the way into the UV. The IR range from 20 μm to 800 nm was dominated by a Drude peak. The screened plasma energy ($\hbar\omega_p$) extracted from the experiment at $\varepsilon_1(\omega) = 0$ was (1.98 ± 0.03) eV. This value was smaller than the reduced plasma energy of 2.15 eV[52] found from DFT. Taking the mass renormalization due to electron correlation effects into account from the comparison of band widths of $SrNbO_3$ calculated by DFT and DMFT, the theoretical value of the reduced plasma frequency is corrected to a smaller value of 1.82 eV. The experimental determination of renormalization constant Z_k from electron correlation effects extracted from the extended Drude model[62,63] was somewhat higher ($Z_k = 0.89 \pm 0.02$) than the theoretically prediced value of 0.72 (see Supplementary Note 2 and 3). Using the Z_k value extracted from experiment gave a corrected reduced plasma frequency of (1.91 ± 0.04) eV, which was in better agreement to the measured screened plasma frequency, indicating that the calculated correlation strenght might be slighlty overestimated.

In the case of $SrNbO_3$ films the correlation induced red-shift was not sufficient to push the carrier reflection edge completely into the IR range, but it helped increasing the transparency within the visbible spectrum at long wavelengths. It is shown in Fig. 2f that the main interband absoption edge was experimentally found at around 4.8 eV (~260 nm), in very good agreement with DFT predictions. Compared to $SrVO_3$, the interband absorption of $SrNbO_3$ was blue-shifted by over 1.5 eV into the UV range. The real and imaginary part of the dielectric function experimentally determined for the $SrNbO_3$ films were small in the visible and UV region up to the absorption edge near 4.8 eV, indicating a relatively low optical absorption coefficient. The small absorption peak at ~2.7 eV obtained in the DFT calculation was originated by a weak interband transition from the t_{2g} to the e_g band. A similar peak was also predicted for $SrVO_3$, but was not experimentally found in either material system. It is not clear why this absorption peak was not measured for $SrNbO_3$ films, and we speculate that the sizeable defect concentration present in the films, which gave rise to relatively low RRR values, also affected the optical properties.

Discussion

The performance of $SrNbO_3$ as transparent conductor was evaluated using the Figure of Merit (Φ_{TC}) proposed by Haacke[64] $\Phi_{TC} = T^{10}/R_s$ with optical transmittance T and sheet resistance R_s. Figure 3a shows the film thickness dependence of Φ_{TC} calculated in the visible range (400–700 nm), and for the UV spectrum from 260 to 320 nm, encompassing the entire UVB range (280–315 nm), along with results from $SrVO_3$ and ITO[45].

The transmittance of the films were calculated from the dielectric function by assuming normal incidence and a free-standing film including surface reflections and multiple interference effects (see Supplementary Note 4). Since the transmittance varied with wavelength the values used were averaged over the spectrum of interest. Thickness-dependent effects on sheet resistance, such as surface and grain boundary scattering were considered in the calculation as well (see Supplementary Note 5). First, the discussion is focused on the performance of $SrNbO_3$ in this visible spectrum. Maximum Φ_{TC} values of $5 \times 10^{-3}\ \Omega^{-1}$ were found at a film thickness of 10 nm, about a factor of two higher than $SrVO_3$ at similar thickness, and a factor of three higher than the best ITO with Φ_{TC} of about $1.6 \times 10^{-3}\ \Omega^{-1}$ at a thickness of 150 nm[45]. The pronounced minimum in Φ_{TC} of ITO was due to constructive interference of light reflected at both surfaces of a freestanding film. The higher Φ_{TC} values of $SrNbO_3$ and the shift of the maximum of the Φ_{TC} curve toward larger thickness compared to $SrVO_3$ was indicative that the optical properties of $SrNbO_3$ were better. Figure 3b shows a direct comparison of the transmission calculated from the dielectric function for 10-nm-thick $SrNbO_3$ and $SrVO_3$ films. While $SrNbO_3$ has a lower transmission in the visible spectrum at longer wavelengths, much higher transmission in the blue spectrum led to an overall higher optical transmission in the visible range. This improvement in optical properties even compensated for the somewhat higher sheet resistance of $SrNbO_3$ (68 Ω/sq.) at a film thickness of 10 nm compared to $SrVO_3$ ($R_s = 45$ Ω/sq.). This shows that $SrNbO_3$ is a competitive transparent conductor material in the visible range. The transmission curve further shows that $SrNbO_3$ has acceptable transmission values in the UV spectrum from 320 to 260 nm. Fig. 3a shows the thickness dependence of Φ_{TC} for $SrNbO_3$, $SrVO_3$ and ITO determined for this UV range. For all transparent conductor materials considered the figure of merits were smaller and the maximum of the Φ_{TC} curves shifted towards smaller film thickness, indicating a reduced optical performance in the UV compared to the visible spectrum. The effect was much less for

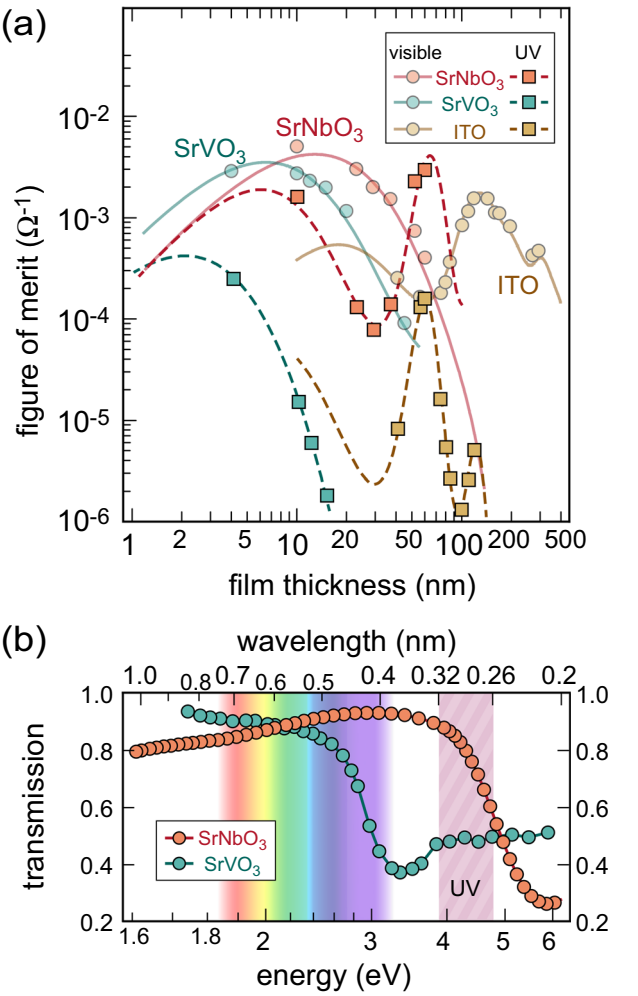

Fig. 3 Comparison of transparent conductor performance. a Figure of Merit Φ_{TC} vs. film thickness for transparent conductors $SrNbO_3$, $SrVO_3$, and indium-tin oxide (ITO) in visible range (400–700 nm, circles) and in the ultraviolet (UV) range (260–320 nm, squares). Experimental data for ITO and $SrVO_3$ were calculated using data from[55,70] and[45], respectively. **b** Transmission of 10-nm-thick freestanding films of $SrNbO_3$ and $SrVO_3$. Rainbow color highlight the visible range, the shaded region labeled UV indicates the spectral range used to calculate figure of merit in the UV shown in **a**.

$SrNbO_3$ films, specifically the Φ_{TC} value for 10-nm-thick films were still above $10^{-3}\ \Omega^{-1}$ and thus comparable with ITO performance in the visible. In contrast, 10-nm-thick $SrVO_3$ the Φ_{TC} was reduced by about two orders of magnitude, rendering it unsuitable for UV applications. ITO had a maximum Φ_{TC} at a thickness of ~60 nm, albeit an order of magnitude lower than the highest Φ_{TC} measured for $SrNbO_3$. The figure of merit for ultra-wide band gap semiconductors like Ga_2O_3 were estimated to be in the mid $10^{-7}\ \Omega^{-1}$ range due to their low electrical conductivity. Furthermore, large dopant concentration of Sn in β-Ga_2O_3 on the order of 10% resulted in a room temperature resistivity of only about $10^{-1}\ \Omega$ cm with carrier mobilities of ~50 $cm^2\ V^{-1}\ s^{-1}$ and a low carrier concentration of about $10^{18}\ cm^{-3}$[48]. Increasing amounts of Sn caused a red-shift of the fundamental absorption edge from 266 to 298 nm in the material, which we attributed to a lattice expansion of the host semiconductor due to the larger size of Sn and an associated decrease of band gap.

In conclusion, $SrNbO_3$ thin films were proposed and experimentally confirmed as high-performance UV transparent

conductors with superior properties in the spectral range from 260 to 320 nm. DFT and DMFT calculations and direct comparison with $SrVO_3$ revealed that the conduction band of $SrNbO_3$ is energetically more isolated from the conduction band. Despite a weaker electron correlation effect the reduced plasma frequency was sufficiently small to open a transparent window that ranged from the visible deep into the UV range due to considerable blue-shift of the interband absorption edge to about 4.8 eV, which is comparable to those of Ga_2O_3 and $ZnGa_2O_4$. Spectroscopic ellipsometry and transport measurements confirmed the theoretical predictions by DFT and DMFT, and subtantiated the potential of the correlated metal $SrNbO_3$ as high performance transparent electrode material for UV application. The rare combination of high transmission and high conductivity of $SrNbO_3$ facilitates the improvement of existing UV LEDs suffering from poor EQEs, enabling energy efficient, long lasting, high performance, portable and environmentally benign solid state lighting solutions for UV sanitation, biomolecule sensing, UV phototherapy, UV curing, UV photolithography and high sensitivity solar blind detector technology.

Methods

Computational methods. First principles Kohn Sham calculations were performed using the Linearized Augmented Plane Wave approach as implemented in the Wien2K[50]. A $25 \times 25 \times 25$ MP grid was used to converge the density of states[65], but in the other calculations a $12 \times 12 \times 12$ grid provides good convergence. Fully charge self consistent, DFT + DMFT calculations are performed using the EDMFTF package (formerly known as DMFT-Wien2K) that uses the Luttinger–Ward functional[51,66,67]. On-site Coulomb interaction in DMFT is taken into account by $U = 6$ eV, in addition to an on-site Hund's coupling of $J = 0.7$ eV. Nominal double counting is used, which is known to give reasonable agreement with experiment in the early d^1 transition metal oxides. The on-site self energy obtained from DMFT has vanishingly small imaginary part on the Fermi level, and its real part is linear, hence the Fermi liquid approach used in the text is valid.

Sample growth and X-ray diffraction. The $SrNbO_3$ films were grown on (100) plane of $KTaO_3$ single crystal substrate by pulsed laser deposition. Details of the film growth condition were reported elsewhere[68]. In short, a sintered pellet of $Sr_2Nb_2O_7$ placed in a vacuum chamber was irradiated by KrF excimer laser ($\lambda =$ 248 nm). The $KTaO_3$ substrates were heated at 700 °C by using an infrared lamp heater. $SrNbO_3$ films were grown by other groups with comparable properties when grown under oxygen deficient conditions[69]. Crystal structure and thicknesses of the thin films were examined by X-ray diffraction (XRD) and X-ray reflectivity using a four-axis diffractometer (Bruker AXS, D8 Discover) with a 2D area detector or a 1D array detector. Details of the XRD results are provided in Supplementary Note 6.

Optical and electrical characterization. Spectroscopic ellipsometry measurements were performed at room temperature to determine the optical properties of $SrNbO_3$ thin films. Ellipsometry spectra in (Ψ,Δ) were collected for $KTaO_3$ substrate, prior to measurements on $SrNbO_3$ films. The (Ψ,Δ) spectra were then collected for $SrNbO_3$ thin films with thicknesses of 10, 23, and 29 nm at incidence angles of 50°, 60°, and 70° using M-2000 Ellipsometer (J.A.Woollam Co., spectral range: 0.734–5.043 eV) and IR-VASE Ellipsometer (J.A.Woollam Co., spectral range: 0.044–0.814 eV), and at the incidence angle of 65.23° using M-2000F Focused Beam Ellipsometer (J.A.Woollam Co., spectral range: 1.242–6.458 eV). All the data collected was appended and modeled with CompleteEase software (J.A. Woollam Co.). Detailed information on ellipsometry modeling and table of oscillators are listed in Supplementary Note 7. Electrical transport measurements were performed at varying temperatures using van der Pauw (VdP) geometry in a Quantum Design Physical Properties Measurement System with a source current of 500 μA. Number of carriers and mobility were determined through Hall measurements in VdP geometry in magnetic field strengths of up to ±8 T applied perpenddicular to the film plane. Sample quality was verified by measuring resistivity from room temperature down to 2.2 K to determine the RRR.

Data availability

All relevant data are available from the corresponding author.

Received: 2 January 2020; Accepted: 11 May 2020;
Published online: 01 June 2020

References

1. Biyikli, N. et al. Solar-blind AlGaN-based Schottky photodiodes with low noise and high detectivity. *Appl. Phys. Lett.* **81**, 3272–3274 (2002).
2. Decker, C., Viet, T. N. T., Decker, D. & Weber-Koehl, E. UV-radiation curing of acrylate/epoxide systems. *Polymer* **42**, 5531–5541 (2001).
3. Hargis, P. J. et al. Ultraviolet fluorescence identification of protein, DNA, and bacteria. in *Optical Instrumentation for Gas Emissions Monitoring and Atmospheric Measurements* (eds Leonelli, J., Killinger, D. K., Vaughan, W. & Yost, M. G.) vol. 2366 147 (SPIE, 1995).
4. Song, K., Mohseni, M. & Taghipour, F. Application of ultraviolet light-emitting diodes (UV-LEDs) for water disinfection: a review. *Water Res.* **94**, 341–349 (2016).
5. Engelmann, G. & Reichl, H. High depth to width aspect ratios in thick positive photoresist layers using near UV lithography. *Microelectron. Eng.* **17**, 303–306 (1992).
6. Morison, W. L. *Phototherapy and Photochemotherapy for Skin Disease*. 3rd edn. (Taylor and Francis Group, Boca Raton, 2005).
7. Hockberger, P. E. A history of ultraviolet photobiology for humans, animals and microorganisms. *Photochem. Photobiol.* **76**, 561–579 (2002).
8. Schreiner, M. et al. UV-B-induced secondary plant metabolites-potential benefits for plant and human health. *Crit. Rev. Plant Sci.* **31**, 229–240 (2012).
9. Bettles, T. et al. UV light emitting diodes; their applications and benefits. *Int. Ultrav. Assoc. N.* **9**, 11–15 (2007).
10. Kneissl, M. & Rass, J. in *III-Nitride Ultraviolet Emitters*, 1–25 (Springer, 2016).
11. Edmond, J. A. & Kong, H.-S. Blue light-emitting diode with high external quantum efficiency. US patent US5416342A (1995).
12. Gauck, H. et al. External radiative quantum efficiency of 96% from a GaAs/GaInP heterostructure. *Appl. Phys. A* **64**, 143–147 (1997).
13. Krames, M. R. et al. High-power truncated-inverted-pyramid $(Al_xGa_{1-x})_{0.5}In_{0.5}P$/GaP light-emitting diodes exhibiting> 50% external quantum efficiency. *Appl. Phys. Lett.* **75**, 2365–2367 (1999).
14. Sakuta, H. et al. Near-ultraviolet LED of the external quantum efficiency over 45% and its application to high-color rendering phosphor conversion white LEDs. *J. Light Vis. Environ.* **32**, 39–42 (2008).
15. Jiao, Q. Q. et al. Capability of GaN based micro-light emitting diodes operated at an injection level of kA/cm^2. *Opt. Express* **23**, 16565–16574 (2015).
16. Zhang, J. et al. Milliwatt power deep ultraviolet light-emitting diodes over sapphire with emission at 278 nm. *Appl. Phys. Lett.* **81**, 4910–4912 (2002).
17. Hirayama, H., Tsukada, Y., Maeda, T. & Kamata, N. Marked enhancement in the efficiency of deep-ultraviolet AlGaN light-emitting diodes by using a multiquantum-barrier electron blocking layer. *Appl. Phys. Express* **3**, 031002 (2010).
18. Kolbe, T. et al. Improved injection efficiency in 290 nm light emitting diodes with Al (Ga) N electron blocking heterostructure. *Appl. Phys. Lett.* **103**, 031109 (2013).
19. Kueller, V. et al. Modulated epitaxial lateral overgrowth of AlN for efficient UV LEDs. *IEEE Photonics Technol. Lett.* **24**, 1603–1605 (2012).
20. Nam, K. et al. Mg acceptor level in AlN probed by deep ultraviolet photoluminescence. *Appl. Phys. Lett.* **83**, 878–880 (2003).
21. Chichibu, S. F. et al. Origin of defect-insensitive emission probability in In-containing (Al, In, Ga) N alloy semiconductors. *Nat. Mater.* **5**, 810 (2006).
22. Tamura, K. et al. InGaN-based light-emitting diodes fabricated with transparent Ga-doped ZnO as ohmic p-contact. *Phys. Status Solidi A* **201**, 2704–2707 (2004).
23. Kim, H. et al. Electrical, optical, and structural properties of indium–tin–oxide thin films for organic light-emitting devices. *J. Appl. Phys.* **86**, 6451–6461 (1999).
24. Ohta, H. et al. Highly electrically conductive indium–tin–oxide thin films epitaxially grown on yttria-stabilized zirconia (100) by pulsed-laser deposition. *Appl. Phys. Lett.* **76**, 2740–2742 (2000).
25. Park, S.-H. et al. Roll-to-roll sputtered ITO/Cu/ITO multilayer electrode for flexible, transparent thin film heaters and electrochromic applications. *Sci. Rep.* **6**, 33868 (2016).
26. Kim, Y. C. et al. Bending stability of flexible amorphous IGZO thin film transistors with transparent IZO/Ag/IZO oxide–metal–oxide electrodes. *J. Alloy. Compd.* **688**, 1108–1114 (2016).
27. Tadatsugu, M. Substitution of transparent conducting oxide thin films for indium tin oxide transparent electrode applications. *Thin Solid Films* **516**, 1314–1321 (2008).
28. Tadatsugu, M. Transparent conducting oxide semiconductors for transparent electrodes. *Semicond. Sci. Technol.* **20**, S35 (2005).
29. Yun, J. Ultrathin metal films for transparent electrodes of flexible optoelectronic devices. *Adv. Funct. Mater.* **27**, 1606641 (2017).
30. Ghosh, D. et al. Widely transparent electrodes based on ultrathin metals. *Opt. Lett.* **34**, 325–327 (2009).
31. Zhang, C. et al. High-performance doped silver films: overcoming fundamental material limits for nanophotonic applications. *Adv. Mater.* **29**, 1605177 (2017).

32. Orita, M., Ohta, H., Hirano, M. & Hosono, H. Deep-ultraviolet transparent conductive β-Ga_2O_3 thin films. *Appl. Phys. Lett.* **77**, 4166–4168 (2000).
33. Garten, L. M. et al. Structure property relationships in gallium oxide thin films grown by pulsed laser deposition. *MRS Commun.* **6**, 348–353 (2016).
34. Omata, T., Ueda, N., Ueda, K. & Kawazoe, H. New ultraviolet-transport electroconductive oxide, $ZnGa_2O_4$ spinel. *Appl. Phys. Lett.* **64**, 1077–1078 (1994).
35. Hrong, R.-H. et al. Transparent electrode design for AlGaN deep-ultraviolet light-emitting diodes. *Opt. Express* **25**, 32206–32213 (2017).
36. Onuma, T. et al. Valence band ordering in β-Ga_2O_3 studied by polarized transmittance and reflectance spectroscopy. *Jpn. J. Appl. Phys.* **54**, 112601 (2015).
37. Oshima, T. et al. Epitaxial growth of wide-band-gap $ZnGa_2O_4$ films by mist chemical vapor deposition. *J. Cryst. Growth* **386**, 190–193 (2014).
38. Wierer, J. et al. High-power AlGaInN flip-chip light-emitting diodes. *Appl. Phys. Lett.* **78**, 3379–3381 (2001).
39. Shatalov, M. et al. AlGaN deep-ultraviolet light-emitting diodes with external quantum efficiency above 10%. *Appl. Phys. Express* **5**, 082101 (2012).
40. Kinoshita, T. et al. Deep-ultraviolet light-emitting diodes fabricated on AlN substrates prepared by hydride vapor phase epitaxy. *Appl. Phys. Express* **5**, 122101 (2012).
41. Fujioka, A. et al. Improvement in output power of 280-nm deep ultraviolet light-emitting diode by using AlGaN multi quantum wells. *Appl. Phys. Express* **3**, 041001 (2010).
42. Takano, T. et al. Deep-ultraviolet light-emitting diodes with external quantum efficiency higher than 20% at 275 nm achieved by improving light-extraction efficiency. *Appl. Phys. Express* **10**, 031002 (2017).
43. Chae, D. et al. AlGaN-based ultraviolet light-emitting diodes using fluorine-doped indium tin oxide electrodes. *Appl. Phys. Lett.* **100**, 081110 (2012).
44. Lee, T. H. et al. Highly efficient deep-UV light-emitting diodes using AlN-based deep-UV-transparent glass electrodes. *ACS Appl. Mater. Interfaces* **9**, 43774–43781 (2017).
45. Zhang, L. et al. Correlated metals as transparent conductors. *Nat. Mater.* **15**, 204 (2015).
46. Brahlek, M. et al. Opportunities in vanadium-based strongly correlated electron systems. *MRS Commun.* **7**, 27–52 (2017).
47. Basov, D. N. et al. Electrodynamics of correlated electron materials. *Rev. Mod. Phys.* **83**, 471 (2011).
48. Du, X. et al. Preparation and characterization of Sn-doped β-Ga_2O_3 homoepitaxial films by MOCVD. *J. Mater. Sci.* **50**, 3252–3257 (2015).
49. Li, K. & Xue, D. Estimation of electronegativity values of elements in different valence states. *J. Phys. Chem. A* **110**, 11332–11337 (2006).
50. Blaha, P. et al. *wien2k. An augmented plane wave+ local orbitals program for calculating crystal properties*. (Karlheinz Schwarz, Tech. Universitt Wien, Austria, 2001).
51. Haule, K., Yee, C.-H. & Kim, K. Dynamical mean-field theory within the full-potential methods: electronic structure of $CeIrIn_5$, $CeCoIn_5$, and $CeRhIn_5$. *Phys. Rev. B* **81**, 195107 (2010).
52. Paul, A. & Birol, T. Strain tuning of plasma frequency in vanadate, niobate, and molybdate perovskite oxides. *Phys. Rev. Mater.* **3**, 085001 (2019).
53. Fuchs, K. The conductivity of thin metallic films according to the electron theory of metals. *Math. Proc. Camb. Philos. Soc.* **34**, 100–108 (1938).
54. Sondheimer, E. H. The mean free path of electrons in metals. *Adv. Phys.* **1**, 1–42 (1952).
55. Ellmer, K. Past achievements and future challenges in the development of optically transparent electrodes. *Nat. Photonics* **6**, 809 (2012).
56. Zeng, X. Y., Zhang, Q. K., Yu, R. M. & Lu, C. Z. A new transparent conductor: silver nanowire film buried at the surface of a transparent polymer. *Adv. Mater.* **22**, 4484–4488 (2010).
57. Ahmadi, E. et al. Ge doping of β-Ga_2O_3 films grown by plasma-assisted molecular beam epitaxy. *Appl. Phys. Express* **10**, 041102 (2017).
58. Leedy, K. D. et al. Highly conductive homoepitaxial Si-doped Ga_2O_3 films on (010) β-Ga_2O_3 by pulsed laser deposition. *Appl. Phys. Lett.* **111**, 012103 (2017).
59. Galazka, Z. et al. Ultra-wide bandgap, conductive, high mobility, and high quality melt-grown bulk $ZnGa_2O_4$ single crystals. *APL Mater.* **7**, 022512 (2019).
60. Ashcroft, N. W. & Mermin, N. D. *Solid State Physics*. (Holt, Rinehart and Winston, 1976).
61. O'Connor, B. et al. Transparent and conductive electrodes based on unpatterned, thin metal films. *Appl. Phys. Lett.* **93**, 433 (2008).
62. Basov, D. N. & Timusk, T. Electrodynamics of high-T_c superconductors. *Rev. Mod. Phys.* **77**, 721–779 (2005).
63. Benfatto, L., Cappelluti, E., Ortenzi, L. & Boeri, L. Extended Drude model and role of interband transitions in the midinfrared spectra of pnictides. *Phys. Rev. B* **83**, 224514 (2011).
64. Haacke, G. New figure of merit for transparent conductors. *J. Appl. Phys.* **47**, 4086–4089 (1976).
65. Monkhorst, H. J. & Pack, J. D. Special points for Brillouin-zone integrations. *Phys. Rev. B* **13**, 5188 (1976).
66. Georges, A., Kotliar, G., Krauth, W. & Rozenberg, M. J. Dynamical mean-field theory of strongly correlated fermion systems and the limit of infinite dimensions. *Rev. Mod. Phys.* **68**, 13 (1996).
67. Haule, K. & Birol, T. Free energy from stationary implementation of the DFT + DMFT functional. *Phys. Rev. Lett.* **115**, 256402 (2015).
68. Oka, D. et al. Intrinsic high electrical conductivity of stoichiometric $SrNbO_3$ epitaxial thin films. *Phys. Rev. B* **92**, 205102 (2015).
69. Wan, D. et al. Electron transport and visible light absorption in a plasmonic photocatalyst based on strontium niobate. *Nat. comm.* **8**, 1–9 (2017).
70. Sopra Material Database. *Refractive Index of ITO, Indium Tin Oxide, InSnO*, https://www.filmetrics.com/refractive-index-database/ITO/Indium-Tin-Oxide-InSnO (Filmetrics, 2018).

Acknowledgements

Y.P., J.R., Ar.P., A.l.P., T.B., V.G., and R.E.H. acknowledge support from the National Science Foundation through DMR-1629477 and J.R. from the NSF Graduate Research Fellowship Program under Grant No. DGE1255832. DO acknowledges support from the Japan Society for the Promotion of Science (JSPS) KAKENHI Grant No. 16K05737. Y.H. and T.H. acknowledge support from the JSPS KAKENHI Grant No 16H06441 and 19K22227. We thank Prof. Tomoteru Fukumura of Tohoku University for allowing us to use the pulsed laser deposition equipment and X-ray diffractometer.

Author contributions

Y.P., J.R., T.B., V.G., and R.E.H. conceived the project, Ar.P. and T.B. performed the DFT/DMFT calculations, D.O., Y.H., and T.H. grew the films, J.R. measured the electrical properties, Y.P., J.R. A.l.P., V.G., and R.E.H. performed spectroscopic ellipsometry and analyzed the results, Y.P., J.R., and R.E.H. co-wrote the paper with input and suggestions from all authors.

Competing interests

The authors declare no competing interests.

Additional information

Supplementary information is available for this paper at https://doi.org/10.1038/s42005-020-0372-9.

Correspondence and requests for materials should be addressed to R.E.-H.

Reprints and permission information is available at http://www.nature.com/reprints

Publisher's note Springer Nature remains neutral with regard to jurisdictional claims in published maps and institutional affiliations.

Open Access This article is licensed under a Creative Commons Attribution 4.0 International License, which permits use, sharing, adaptation, distribution and reproduction in any medium or format, as long as you give appropriate credit to the original author(s) and the source, provide a link to the Creative Commons license, and indicate if changes were made. The images or other third party material in this article are included in the article's Creative Commons license, unless indicated otherwise in a credit line to the material. If material is not included in the article's Creative Commons license and your intended use is not permitted by statutory regulation or exceeds the permitted use, you will need to obtain permission directly from the copyright holder. To view a copy of this license, visit http://creativecommons.org/licenses/by/4.0/.

© The Author(s) 2020